

Dependence of interferogram phase on incident wavenumber and phase stability of Doppler asymmetric spatial heterodyne spectroscopy

Ya-Fei Zhang(张亚飞), Yu-Tao Feng(冯玉涛), Di Fu(傅頓), Peng-Chong Wang(王鹏冲), Jian Sun(孙剑), Qing-Lan Bai(白清兰)

Citation: Chin. Phys. B . 2020, 29(10): 104204 . **doi:** 10.1088/1674-1056/ab9de8
Journal homepage: http://cpb.iphy.ac.cn; http://iopscience.iop.org/cpb

What follows is a list of articles you may be interested in

Second-order interference of two independent photons with different spectra

Yu Zhou(周宇), Jian-Bin Liu(刘建彬), Huai-Bin Zheng(郑淮斌), Hui Chen(陈辉), Fu-Li Li(李福利), Zhuo Xu(徐卓)
Chin. Phys. B . 2019, 28(10): 104205 . **doi:** 10.1088/1674-1056/ab3f23

Memory effect evaluation based on transmission matrix calculation

Ming Li(李明), Long-Jie Fang(方龙杰), Lin Pang(庞霖)
Chin. Phys. B . 2019, 28(7): 074207 . **doi:** 10.1088/1674-1056/28/7/074207

Physical manipulation of ultrathin-film optical interference for super absorption and two-dimensional heterojunction photoconversion

Guo-Yang Cao(曹国洋), Cheng Zhang(张程), Shao-Long Wu(吴绍龙), Dong Ma(马冬), Xiao-Feng Li(李孝峰)
Chin. Phys. B . 2018, 27(12): 124202 . **doi:** 10.1088/1674-1056/27/12/124202

Universal form of the power spectrum of the aero-optical aberration caused by the supersonic turbulent boundary layer

Gao Qiong, Yi Shi-He, Jiang Zong-Fu
Chin. Phys. B . 2014, 23(10): 104201 . **doi:** 10.1088/1674-1056/23/10/104201

Multi-wavelength laser active coherent combination

Han Kai,Xu Xiao-Jun,Liu Ze-Jin
Chin. Phys. B . 2012, 21(5): 054205 . **doi:** 10.1088/1674-1056/21/5/054205

Dependence of interferogram phase on incident wavenumber and phase stability of Doppler asymmetric spatial heterodyne spectroscopy*

Ya-Fei Zhang(张亚飞)[1,2], Yu-Tao Feng(冯玉涛)[1,†], Di Fu(傅峘)[1], Peng-Chong Wang(王鹏冲)[1], Jian Sun(孙剑)[1], and Qing-Lan Bai(白清兰)[1]

[1] *Xi'an Institute of Optics and Precision Mechanics, Chinese Academy of Sciences, Xi'an* 710119, *China*
[2] *University of Chinese Academy of Sciences, Beijing* 100049, *China*

(Received 7 January 2020; revised manuscript received 30 April 2020; accepted manuscript online 18 June 2020)

Instrument drifts introduce additional phase errors into atmospheric wind measurement of Doppler asymmetric spatial heterodyne spectroscopy (DASH). Aiming at the phase sensitivity of DASH to instrument drifts, in this paper we calculate the optical path difference (OPD) and present an accurate formula of DASH interferogram. By controlling variables in computational ray-tracing simulations and laboratory experiments, it is indicated that initial phase is directly determined by incident wavenumber, OPD offset and field of view (FOV). Accordingly, it is indicated that retrieved phase of DASH is sensitive to slight structural change caused by instrument drift, which provides the proof of necessary-to-track and -correct phase errors from instrument drifts.

Keywords: atmospheric wind measurement, Doppler asymmetric spatial heterodyne spectroscopy, optical path difference, interference phase

PACS: 42.25.Hz, 07.60.Ly, 42.68.–w **DOI:** 10.1088/1674-1056/ab9de8

1. Introduction

On-orbit measurement of middle and upper atmospheric wind field provides critical data for several applications such as space society, global communication, weather forecasting, and military.[1] Over the last few decades, different techniques have been applied and multiple kinds of instruments have been launched for on-orbit wind observations.[1–5] Doppler asymmetric spatial heterodyne spectroscopy (DASH) is recently developed and has become an interesting candidate.[6] Compared with Michelson and Fabry–Perot techniques, DASH can be built in rugged and compact packages, and provides high etendue and multiline capability.[5] Like other interference imaging techniques, DASH estimates wind velocity according to the Doppler shift of incident atmospheric emission line.[4,5] The Doppler shift is determined by evaluating phase change of measured interferogram relative to the zero-wind reference.[5] However, the Doppler shift caused by atmospheric wind is rather weak. In order to measure the wind speed within useful precision (10 m/s or better), the challenge is to measure the position of one Doppler shifted line or more which has $1/3\times10^7$ or less of their wavelength.[4] However, the temperature variety of environment introduces additional errors into phase measurements, such as change of Littrow wavenumber, thermally inducing phase offset and image shift.[7,8] These effects result from the thermal dependence of interferometer components and structure. Effective analysis of phase sensitivity to instrument drift is necessary, and needs to solve the dependence of interferogram phase on all interferometer parameters above.

There have been several studies of accurate formula of DASH interferogram. In 2006, Englert *et al.*[5] first developed the DASH concept and proposed an analytic formula of recorded interferogram. In this formula, the initial phase term depends on the optical path difference (OPD) offset and the difference between incident wavenumber and the Littrow wavenumber of diffraction gratings. In 2015, Fei *et al.*[9] derived a new formula of DASH interferogram based on calculation of OPD. Their only difference is that the phase term is directly determined by incident wavenumber rather than wavenumber difference. In 2018, Liu *et al.*[10] innovated the effective OPD to correct the phase term in filed-widened DASH (FW-DASH) configuration. It is worth mentioning that applying the effective OPD to wind retrieval produces a more accurate result.

These researches determined the phase term theoretically by considering axial incident light. However, the optical path of off-axial incident light is different from that of axial light. In this way, the interferogram is also affected by field of view (FOV) of the interferometer.

Through tracing optical path and calculating OPD, not only axial but also off-axial formula of DASH interferogram is presented in this paper. And then the computational ray-

*Project supported by the National Natural Science Foundation of China (Grant No. 41005019), the Fund from the Chinese Academy of Scieneces for West Yong Scientists (Grant No. XAB 2016A07), and the Natural Science Basic Research Program of Shaanxi Province, China (Grant No. 2019JQ-931).

†Corresponding author. E-mail: fytciom@126.com

© 2020 Chinese Physical Society and IOP Publishing Ltd

tracing simulations and laboratory experiments provide practical specification that determines the dependence of interferogram phase on interferometer parameters. Discussion on phase decomposition of interferogram indicates that the initial phase term is extremely sensitive to instrument drifts, which shows the necessity of effective thermal control.

2. Theoretical analysis

The DASH works based on the Michelson interference principle as shown in Fig. 1(a). When light enters into a DASH interferometer, it is firstly divided into two optical paths by the beam splitter. Then two light beams from both paths are returned by the Littrow gratings. They meet and generate Fizeau fringes on the image plane.

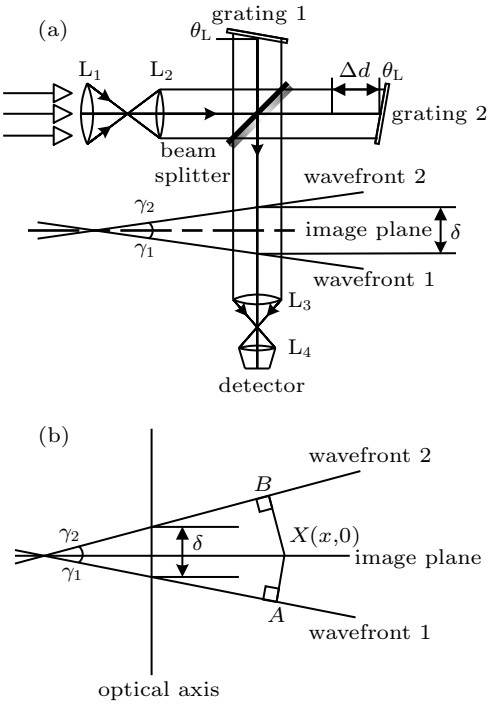


Fig. 1. (a) Schematic diagram of typical DASH interferometer, where L_1 and L_2 are collimating lenses. L_3 and L_4 are imaging lenses, gratings 1 and 2 are tilted by a Littrow angle θ_L, Δd is the asymmetric offset of two optical arms. Outgoing wavefronts have the same phase. (b) Schematic diagram of the calculation of OPD. Because wavefronts 1 and 2 have the same phase, the OPD at point X on image plane can be obtained by $|BX|+|XA|$.

According to the interference principle, the intensity of interferogram recorded by the detector can be written as[11]

$$I(D)=\frac{1}{2}I_0\left[1+\cos\left(2\pi\sigma\cdot D\right)\right], \tag{1}$$

where I_0 is the intensity and σ is the wavenumber of incident light, and D is the distribution of OPD on the image plane. As shown in Fig. 1(b), for a DASH interferometer, OPD distribution comes from the inclination and the optical path delay δ. It can be calculated by

$$D=(\sin\gamma_1+\sin\gamma_2)\cdot x+\delta, \tag{2}$$

where x is the position on image plane. An approximation of $(\sin\gamma_1+\sin\gamma_2)/(\tan\gamma_1+\tan\gamma_2)\approx 1$ has been applied to Eq. (2) because the incident angle is quite small due to the limit of FOV.

2.1. Analysis and calculation of interferogram

Substituting Eq. (2) into Eq. (1), the distribution of interference fringes can be clearly determined by using the tilt angle of outgoing wavefronts and the optical path delay. The frequency of interferogram is determined by the tilt angle of outgoing wavefront and the phase is determined by both two factors. Based on the diffraction effect of gratings, tilt angle of outgoing wavefront can be calculated by[12]

$$\begin{cases}\sigma\cos\varphi\cdot\left[\sin\left(\theta_L\pm\beta\right)+\sin\left(\theta_L-\gamma_{1(2)}\right)\right]=2\sigma_L\sin\theta_L,\\ \varphi_{1(2)}=-\varphi,\end{cases} \tag{3}$$

where β is the angle between optical axis and the component of incident light in the dispersion plane, φ is the angle between incident light and the dispersion plane, and σ_L is the Littrow wavenumber.

In order to determine the phase term, an approximation is used to calculate δ in Eq. (2). In this approximation, a wavefront moves along the optical axis, and its speed depends on its tilt angle. For example, the speed of incident wavefront can be determined by $c/(\cos\beta\cdot\cos\varphi)$, where c is the speed of light. Then, the optical path delay can be considered as the distance traveled by wavefront 1 when wavefront 2 has moved $2\Delta d$ in the interval of asymmetric OPD offset as shown in Fig. 2.

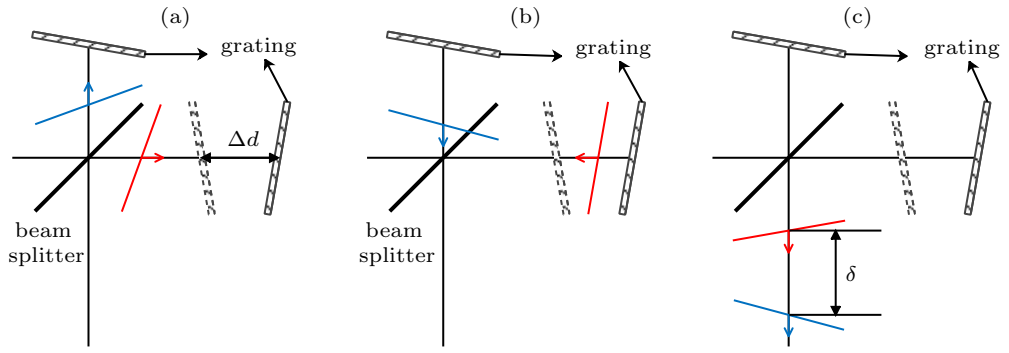


Fig. 2. Schematic diagram of wavefronts movement approximation, where red and blue lines represent wavefronts and arrows denote the direction of approximated wavefronts.

In the axial case, light in each of the two arms is incident on grating along the optical axis, so that the tilt angles of two exit wavefronts are numerically equal. The optical path delay can be calculated from $\delta = (1/\cos\gamma_1 + 1)\cdot\Delta d$, and then the axial interferogram can be written as

$$I = I_0\left[1+\cos\left\{2\pi\left[4\left(\sigma-\sigma_{\rm L}\right)\tan\theta_{\rm L}\cdot x+2\sigma\cdot\Delta d\right]\right\}\right], \quad (4)$$

where an approximation of $\cos\gamma_1 \approx 1$ has been used.

In the off-axial case, the optical path delay can be calculated from $\delta = (\cos\beta/\cos\gamma_1 + 1)\cdot\Delta d$. Considering the effect of angle φ, the OPD distribution is calculated to be $(\sin\gamma_1+\sin\gamma_2)\cos\varphi\cdot x+\cos\varphi\cdot\delta$ according to Eq. (2). However, unlike the axial case, the final off-axial interferogram is the integration of fringe patterns generated by incident light with various FOV angles smaller than the maximum FOV angle $\Omega_{\rm max}$. The maximum FOV solid angle is determined by $\Omega_{\rm max} = \pi/2W\sigma\sin\theta_{\rm L}$, where W is the width of grating.[12] The intensity $\mathrm{d}I$ with viewing solid angle $\mathrm{d}\Omega$ can be calculated from

$$\begin{aligned}\mathrm{d}I = I_0\Bigg(1+\cos\Bigg(2\pi\Bigg\{4\Bigg[\left(1-\frac{\Omega}{2\pi}\right)\sigma'-\frac{\Omega}{2\pi}\sigma_{\rm L}\Bigg]\\ \times\tan\theta_{\rm L}\cdot x+\left(2-\frac{\Omega}{2\pi}\right)\sigma\cdot\Delta d\Bigg\}\Bigg)\Bigg)\mathrm{d}\Omega, \quad (5)\end{aligned}$$

where $\sigma' = \sigma - \sigma_{\rm L}$. Thus substituting $\Omega \approx \beta^2+\varphi^2$[12] into Eq. (6), integrating the resulting equation over the FOV solid angle from 0 to $\Omega_{\rm max}$, the off-axial interferogram can be obtained as follows:

$$\begin{aligned}I = I_0\cdot\Omega_{\rm max}\Bigg[1+\sin c\left(\frac{4\Omega_{\rm max}\sigma\tan\theta_{\rm L}\cdot x+\Omega_{\rm max}\sigma\cdot\Delta d}{2\pi}\right)\\ \times\cos\Bigg(2\pi\Bigg\{4\Bigg[\left(1-\frac{\Omega_{\rm max}}{4\pi}\right)\sigma'-\frac{\Omega_{\rm max}}{4\pi}\sigma_{\rm L}\Bigg]\tan\theta_{\rm L}\cdot x\\ +\left(2-\frac{\Omega_{\rm max}}{4\pi}\right)\sigma\cdot\Delta d\Bigg\}\Bigg)\Bigg]. \quad (6)\end{aligned}$$

The sinc function in Eq. (6) reduces contrast or visibility of interferogram. This reduction effect depends on optical path offset Δd and maximum FOV solid angle $\Omega_{\rm max}$. It means that the phase sensitivity and optical throughout are limited in a non-field-widen DASH interferometer. For real observations, the application of field-widen technique is necessary.

2.2. Computational ray-tracing simulation

Equation (6) is a general expression of interferogram generated by DASH without field-widened. According to Eqs. (5) and (6), the spatial frequency and initial phase of DASH interferogram are determined by wavenumber, FOV and OPD offset. In order to verify this effect, computation simulations were performed by using a ray-tracing model built based on the configuration shown in Fig. 1. In this model, the Littrow wavenumber was fixed at 15840 cm^{-1} (wavelength 631.32 nm). Meanwhile, the focal length of fore-lens was 120 mm, and the image magnification of image-lens was −0.80. The simulated interferograms were subjected to column averaging and cosine-fitting to obtain their spatial frequency and initial phase. And then these results were numerically compared with calculated results as shown in Figs. 3 and 4. Calculation is performed according to Eq. (5) in order to avoid significantly dropping in contrast of interferogram.

Firstly, simulation aims at the effect of FOV solid angle on spatial frequency and initial phase. The OPD offset was fixed at 300 nm. The incident wavenumber was set to be 15803 cm^{-1} (wavelength 632.80 nm), and the effect of line shape was ignored. Meanwhile, another wavenumber of 15873 cm^{-1} (wavelength 630.00 nm) was used as a reference. Various FOV solid angles were achieved by changing the radius of light source which was set to be a circular array made up of 36 identical point sources. The limit of radius could be calculated to be 0.90 mm by using the maximum FOV solid angle and the focal length of fore-lens. In order to reduce the influence of random errors, five interferograms were generated in each simulation.

Numerical comparisons in Fig. 3 show the proximity of simulated interferograms and the interferograms calculated according to Eq. (5). Errors are due to the fact that the random generation of rays results in small random drift of interferogram. With the increase of FOV angle, the deterioration of the interferogram quality leads the randomness of the simulation results to increase.

Secondly, simulations were performed for the effect of OPD offset on interferogram phase. The FOV angle was fixed at zero. Two lines with the same wavenumber in the previous step were used to generate interferograms. The OPD offset was continuously changed to obtain various phases for comparison.

Comparisons in Fig. 4 show the consistence between calculated and simulated results. It is shown that interferogram phase is proportional to the OPD offset. And the slope reflects that the phase is directly determined by wavenumber rather than wavenumber difference. Errors result from the randomness of rays and are small enough to be neglected.

Overall, the consistence of calculations and simulations preliminarily verify the description of DASH interferogram without field widening by Eq. (5). It is indicated that the spatial frequency of DASH interferogram is affected by FOV, which results in decrease of interferogram contrast in the off-axial case. For the phase term, it is also indicated that the OPD offset plays a dominant role while the influence of wavenumber is relatively small.

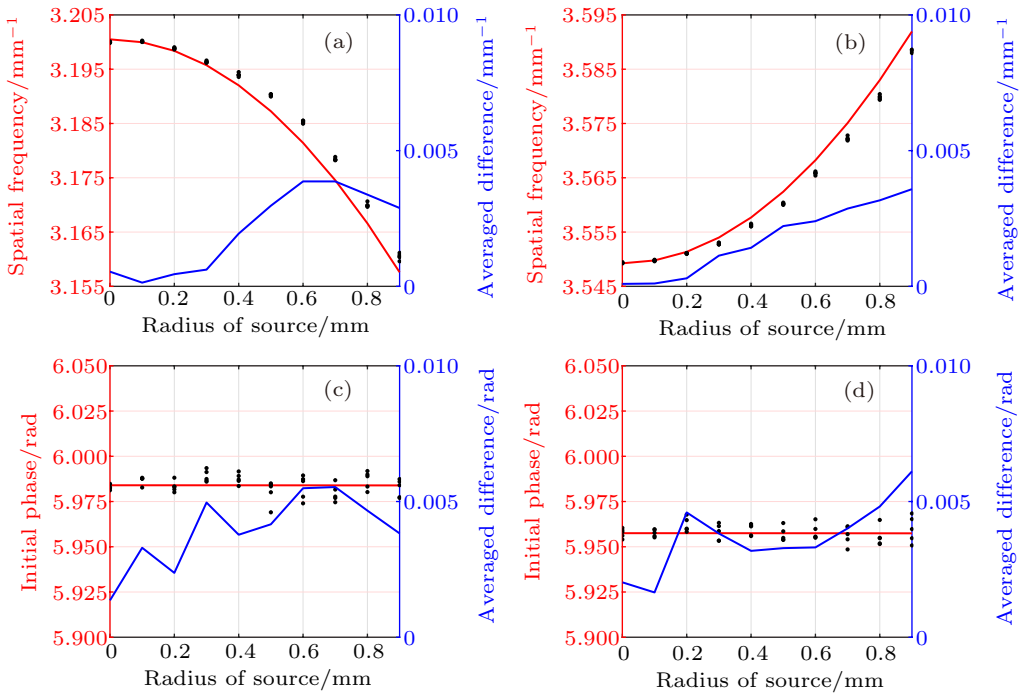


Fig. 3. FOV effects and comparisons at [(a) and (c)] 15873 cm^{-1} and [(b) and (d)] 15803 cm^{-1}. Red lines represent results calculated from Eq. (5). Black dots denote simulation results. Blue lines indicate averaged difference between calculation and simulation results. Averaged difference is obtained by averaging the absolute values of all differences.

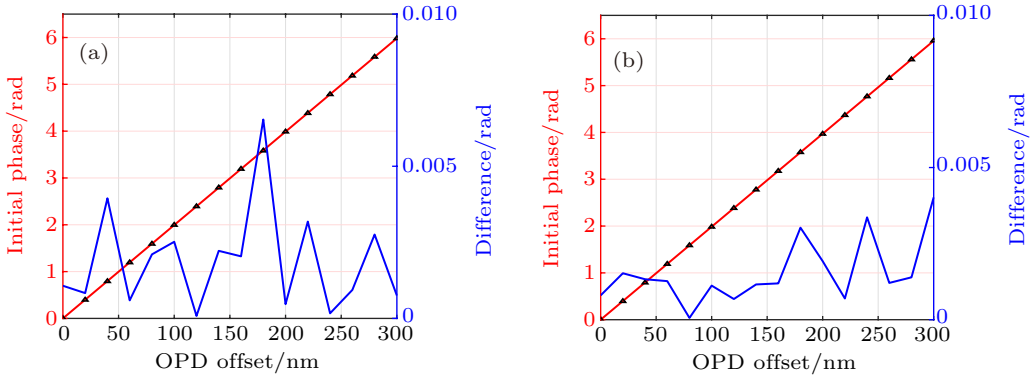


Fig. 4. Phase comparisons of OPD offset effect (a) at 15873 cm^{-1} and (b) at 15803 cm^{-1}. Red lines represent results calculatedfrom Eq. (5). Black triangles represent simulation results. Blue lines indicate averaged difference between calculation and simulation results.

3. Experiment and discussion

3.1. Experiment on phase variation trend with asymmetric offset

To further verify the phase term of DASH interferogram, a laboratory DASH optical system was set up based on the configuration shown in Fig. 1. But one of gratings with a density of 600 groove/mm was mounted on a linear stage (PI LPS-45, with E-871 PIShift controller) so that the OPD offset could be continuously changed. The system was illuminated by a He–Ne laser source (Thorlabs HNL150LB) and the generated fringes pattern was recorded by an array detector (Vieworks VH-4MG2-MC 20) behind a dual telecentric imaging lens. Prior to the subsequent process, the grating on the linear stage was adjusted to a position quite symmetrical with the other grating, where the contrast of interferogram was nearly the highest.

In order to acquire phase variation with the OPD offset, the grating on linear stage was gradually moved in steps of 5 nm. Five recordings were made after each move, and then these images were averaged to reduce random errors caused by environmental vibrations. An averaged interferogram is shown in Fig. 5(a). There are a slight tilt and distortion in recorded interferogram due to alignment errors and lens aberrations. Regions from the 901st row to the 950th row of interferograms were selected and averaged in vertical direction to improve the signal quality.

The Fourier approach[13] was adopted to obtain fringe phase. Firstly, the analysis signal was processed by a Fourier transform after removing the baseline. Then, the conjugate spectral peak was isolated and inverse transform was performed. Thus a complex-valued fringe signal could be obtained. This signal had the same phase and amplitude as

the original fringes. The raw phase, modulo 2π as shown in blue points in Fig. 5(c), could be retrieved from the complex-valued fringe by using the arc-tangent function. Final phase distribution, a nearly linear function as shown in red points in Fig. 5(c), could be produced by unwrapping the raw phase with the 2π discontinuities removed.[13]

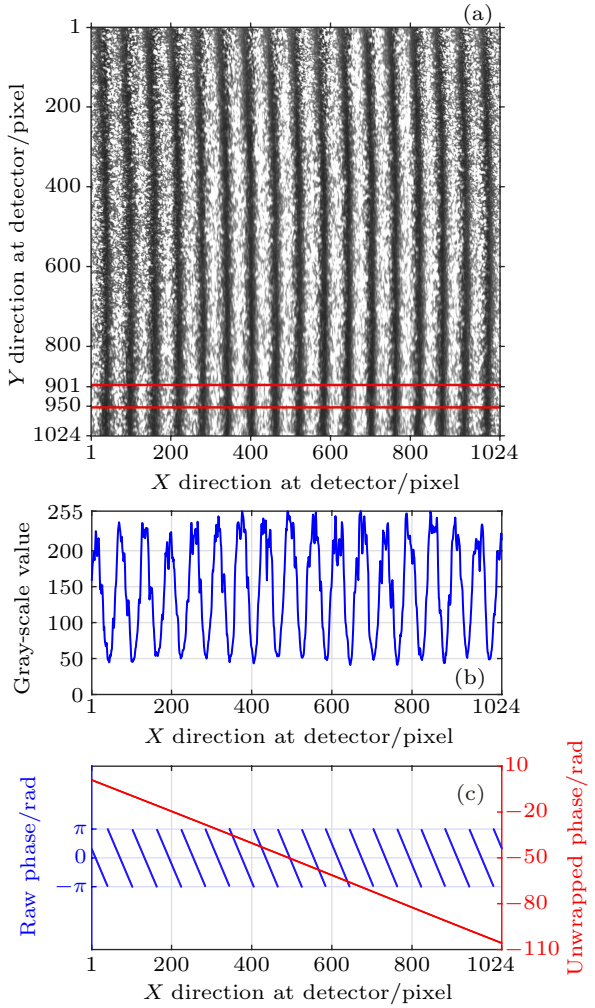


Fig. 5. (a) Averaged interferogram from five recorded pictures. (b) Analysis signal generated from the selected area shown in panel (a). (c) Schematic diagram of inversion phase from analysis signal shown in panel (b). Blue points indicate the retrieved raw phase and red points reptrsent the unwrapped phase.

When the grating on linear stage was gradually moved, phase change shows a nearly linear trend as shown in Fig. 5. The phase change was determined relatively to original position and has been unwrapped. For comparison, the theoretical trend is simultaneously presented, and the experimental result is fitted in the form of a proportional function. The theoretical trend could be calculated from $\Delta\varphi = 4\pi\sigma \cdot \Delta s$, where $\Delta\varphi$ is the phase change and Δs is the change of OPD offset, or the movement of the grating on linear stage.

Comparison in Fig. 5 shows that experimental result is in good agreement with theoretical calculation. The slopes of fitted experimental line and theoretical line are respectively 0.0200 and 0.0199. Meanwhile, the averaged phase change of each step can be calculated to be 0.0989 rad while the theoretical expectation is 0.0993 rad. What needs to be noted is that experimental results in the interval between about 50 nm and 350 nm are not perfectly consistent with linear trend, even abnormal changes appearing at some positions. These errors are due to instability of linear stage whose movement is not always continuously uniform.

3.2. Discussion about phase stability

Through the above simulation and experiment, the theoretical analysis of DASH interferogram is practically verified. Accordingly, the phase term is directly determined by incident wavenumber rather than wavenumber difference. The dependence of phase term on incident wavenumber greatly affects the phase stability of DASH.

In an interference system, according to the optical Doppler theory, the Doppler phase term, meaning the phase shift of a single emission line, can be written as[5]

$$\delta\varphi = 2\pi \cdot D \cdot \sigma \frac{v}{c}, \tag{7}$$

where v is the Doppler velocity. According to the Fourier approach, the phase term can be calculated from the ratio of the imaginary part to the real part of the complex-valued fringe pattern,[5]

$$2\pi\kappa \cdot x + \Phi_0 + \delta\varphi = \arctan \frac{\Im(I_D)}{\Re(I_D)}, \tag{8}$$

where x is the location on the detector, $\kappa = 4(\sigma - \sigma_L)\tan\theta_L$ is the spatial frequency for line center, $\Phi_0 = 4\pi\sigma\Delta d$ is the initial phase term, and I_D is the complex-valued fringe. After subtracting the zero-wind phase $2\pi\kappa \cdot x + \Phi_0$, the relative velocity of the emitter and interferometer can be calculated according to Eq. (7).

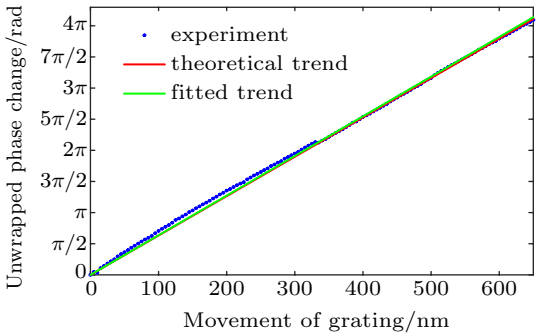


Fig. 6. Phase variations at 512nd pixel when grating on the linear stage is gradually moved.

Instruments drifts cause OPD offset to change Δd, which gives rise to additional phase error affecting wind retrieval. According to Eq. (8), the retrieved phase consists of three parts, *i.e.*, the frequency term $2\pi\kappa \cdot x$, the Doppler phase term $\delta\varphi$, and the initial phase term Φ_0.

Firstly, the frequency term in the zero-wind phase is independent of OPD offset. Changes of OPD offset caused by instrument drifts will not give rise to additional errors.

Secondly, the Doppler phase term depends on the OPD D according to Eq. (7). In real application, OPD changes originating from instrument drifts are some orders of magnitude smaller than OPD itself. Therefore, the Doppler phase error from instrument drifts is commonly ignored.

Thirdly, the initial phase term is linearly related to the wavenumber and OPD offset. For airglow emission lines commonly used in atmospheric wind measurement, the order of magnitude of wavenumber makes initial phase term extremely sensitive to slight changes of OPD offset. That is why the interference phase of DASH is sensitive to thermal drift.

Accordingly, determining accurate zero-wind phase is critical for wind measurements. This can be achieved from two aspects. On the one hand, with the multiline capability,[5] a DASH interferometer can simultaneously accept another known, non-Doppler-shifted reference line, which allows the zero-wind phase to be tracked. On the other hand, application of thermal methods contributes to the reduction of instrument drifts. Thermal compensation is an effective approach to implementing reasonable structural design. Besides, active thermal control also works but requires some additional mechanical components. Some of these techniques have been implemented in previous instruments such as WINDII,[14,15] which provides a reference for application in DASH.

4. Conclusions

Aming at the determination of the phase term, in this paper we theoretically calculate and practically verify the DASH interferogram without field widening. Theoretical analysis is in good agreement with results obtained from both simulations and experiments. Therefore, the initial phase term of DASH interferogram is directly determined by OPD offset, FOV solid angle, and incident wavenumber. Among these three factors, the influence of FOV solid angle is relatively small. However, due to the order of magnitude of wavenumber for emission lines commonly used in wind measurements, the initial phase is extremely sensitive to micro change of OPD offset caused by instrument drifts. This shows the necessity of applying effective approaches to tracking instrument drifts, thermal compensation or active thermal control to determine the zero-wind phase with sufficient accuracy. In this paper, due to increasing complexity of FW-DASH optical paths, only DASH interferogram is studied. The accurate phase term of an FW-DASH interferometer is to be solved.

References

[1] Zhang C, Zhao B, Xiangli B and Li Y 2006 *Optik* **117** 265
[2] Hersom C H and Shepherd G G 1995 *Appl. Opt.* **34** 2871
[3] Shepherd G G 1996 *Appl. Opt.* **35** 2764
[4] Englert C R, Harlander J M, Babcock D D, Stevens M H and Siskind D E 2006 *Atmospheric Optical Modeling, Measurement, and Simulation II*, September 1, 2006. San Diego, California, USA, p. 63030T
[5] Englert C R, Babcock D D and Harlander J M 2007 *Appl. Opt.* **46** 7297
[6] Englert C R, Brown C M, Bach B, Bach E, Bach K, Harlander J M, Seely J F, Marr K D and Miller I 2017 *Appl. Opt.* **56** 2090
[7] Englert C R, Harlander J M, Emmert J T, Babcock D D and Roesler F L 2010 *Opt. Express* **18** 27416
[8] Englert C R, Harlander J M, Brown C M, Marr K D, Miller I J, Stump J E, Hancock J, Peterson J Q, Kumler J, Morrow W H, Mooney T A, Ellis S, Mende S B, Harris S E, Stevens M H, Makela J J, Harding B J and Immel T J 2017 *Space Sci. Rev.* **212** 553
[9] Fei X, Feng Y, Bai Q, Xie N, Li Y, Yan P and Sun J 2015 *Acta Opt. Sin.* **35** 0422003 (in Chinese)
[10] Liu J, Wei D, Zhu Y, Kaufmann M, Olschewski F, Mantel K, Xu J and Riese M 2018 *Appl. Opt.* **57** 8829
[11] Perklins C 2013 *Spatial heterodyne spectroscopy: modeling and interferogram processing*, MS Dissertation (Rochester: Rochester Institute of Technology)
[12] Harlander J M 1991 *Spatial heterodyne spectroscopy: Interferometric performance at any wavelength without scanning*, Ph.D. dissertation (Wisconsin: The University of Wisconsin-Madison)
[13] Harlander J M, Englert C R, Marr K D, Harding B J and Chu K T 2019 *Appl. Opt.* **58** 3613
[14] Thuillier G, Gault W, Brun J F, Hersé M, Ward W and Hersom C 1998 *Appl. Opt.* **37** 1356
[15] Shepherd M and Fricke-Begemann C 2004 *Ann. Geophys.* **22** 1513